ACS OMEGA

Open Access

http://pubs.acs.org/journal/acsodf

Article

In Silico and In Vitro Potential of FDA-Approved Drugs for Antimalarial Drug Repurposing against *Plasmodium* Serine Hydroxymethyltransferases

Pitchayathida Mee-udorn, Kochakorn Phiwkaow, Ruchanok Tinikul, Kamonpan Sanachai, Somchart Maenpuen, and Thanyada Rungrotmongkol*

Cite This: *ACS Omega* 2023, 8, 35580−35591

Read Online

ACCESS | Metrics & More | Article Recommendations | Supporting Information

ABSTRACT: Malaria has spread in many countries, with a 12% increase in deaths after the coronavirus disease 2019 pandemic. Malaria is one of the most concerning diseases in the Greater Mekong subregion, showing increased drug-resistant rates. Serine hydroxymethyltransferase (SHMT), a key enzyme in the deoxythymidylate synthesis pathway, has been identified as a promising antimalarial drug target due to its conserved folate binding pocket. This study used a molecular docking approach to screen 2509 US Food and Drug Administration (FDA)-approved drugs against seven *Plasmodium* SHMT structures. Eight compounds had significantly lower binding energies than the known SHMT inhibitors pyrazolopyran(+)-86, tetrahydrofolate, and antimalarial drugs, ranging from 4 to 10 kcal/mol. Inhibition assays testing the eight compounds against *Plasmodium falciparum* SHMT (*Pf*SHMT) showed that amphotericin B was a competitive inhibitor of *Pf*SHMT with a half-maximal inhibitory concentration (IC_{50}) of 106 ± 1 μM. Therefore, a 500 ns molecular dynamics simulation of *Pf*SHMT/PLS/amphotericin B was performed. The backbone root-mean-square deviation of the protein−ligand complex indicated the high complex stability during simulations, supported by its radius of gyration, hydrogen-bond interactions, and number of atom contacts. The appreciable binding affinity of amphotericin B for *Pf*SHMT was indicated by their solvated interaction energy (−11.15 ± 0.09 kcal/mol) and supported by strong ligand−protein interactions (≥80% occurrences) with its essential residues (i.e., Y78, K151, N262, F266, and V365) predicted by pharmacophore modeling and per-residue decomposition free energy methods. Therefore, our findings identify a promising new *Pf*SHMT inhibitor, albeit with less inhibitory activity, and suggest a core structure that differs from that of previous SHMT inhibitors, thus being a rational approach for novel antimalarial drug design.

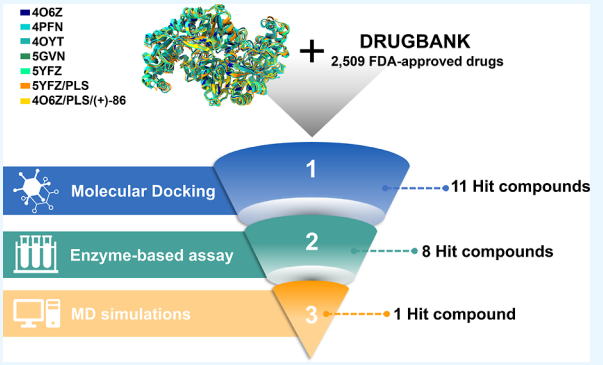

1. INTRODUCTION

Malaria is a mosquito-borne disease that commonly infects humans through five *Plasmodium* species (i.e., *Plasmodium falciparum*, *Plasmodium vivax*, *Plasmodium malariae*, *Plasmodium ovale*, and *Plasmodium knowlesi*).[1−4] Two of these species (*P. falciparum* and *P. vivax*) account for the severe form of malaria worldwide.[5,6] The World Health Organization (WHO) estimated that there were 241 million clinical malaria cases and 627,000 deaths in 2020, a 12% increase from precoronavirus disease 2019 pandemic levels.[7] The available treatments, particularly for *P. falciparum* and *P. vivax* malaria, are artemisinin-based combination therapy (ACT) and chloroquine.[8,9] However, resistance to currently used first-line and other antimalarial drugs has been reported in many regions worldwide, especially in the Greater Mekong subregion.[3,10,11] Therefore, discovering new drugs and targets has become crucial.

Serine hydroxymethyltransferase (SHMT) is a crucial pyridoxal-5′-phosphate (PLP)-dependent enzyme in the deoxythymidylate (dTMP) synthesis pathway, catalyzing the reversible conversion of L-Ser and (6*S*)-tetrahydrofolate (THF) to glycine and 5,10-methylenetetrahydrofolate (CH_2−THF).[12−14] SHMT was identified as the novel antimalarial drug target because of its conserved folate-binding pocket, comprising five loop structures (Figure 1A,B), which is considered a suitable target for novel inhibitors.[15−17] Therefore, drug resistance due to protein mutations should not infrequently occur for this enzyme. In addition, inhibition of SHMT expression or function could be lethal to the *Plasmodium* parasites.[15] In this respect, the discovery of

Received: February 27, 2023
Accepted: September 8, 2023
Published: September 18, 2023

https://doi.org/10.1021/acsomega.3c01309
ACS Omega 2023, 8, 35580−35591

A

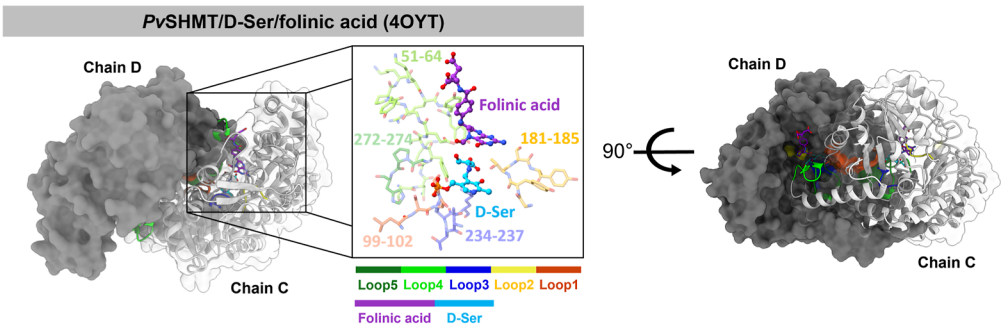

B

	Loop 1				Loop 2					Loop 3				Loop 4																Loop 5		
P. vivax	L	S	G	S	G	Y	T	S	Y	T	T	H	K	S	N	K	Y	S	E	G	Y	P	K	K	R	Y	Y	G	P	H
P. falciparum	L	S	G	S	G	Y	T	S	Y	T	T	H	K	S	N	K	Y	S	E	G	Y	P	H	K	R	Y	Y	G	P	H
Residue No.	99	100	101	102	181	182	183	184	185	234	235	236	237	51	52	53	54	55	56	57	58	59	60	61	62	63	64	272	273	274	

Figure 1. (A) *Pv*SHMT structure bound with folinic acid and D-Ser (Protein Data Bank [PDB]: 4OYT),[15] where chains C and D are visualized as ribbons and surface diagrams, respectively. (B) The *Pv*SHMT binding pocket shares a very high amino acid sequence identity (97%) with that of *Pf*SHMT.[15,23] Note that a different amino acid is shaded in gray. Reproduced with permission from ref 24, Copyright 2022, Journal of Molecular Liquids.

Plasmodium SHMT inhibitors could identify candidates for novel antimalarial drug development.

The traditional drug development process for the *Plasmodium* SHMT target might take years and be very costly.[18] Therefore, drug repurposing could be a suitable strategy to reduce time and investment in novel drug discovery.[18,19] Drug repurposing or drug reprofiling is a rapid process to identify new uses for approved drugs (e.g., US Food and Drug Administration [FDA]-approved drugs) outside the scope of their original medical indication.[20] The failure risk of the drug repurposing method is lower than that of the traditional process because the repurposed drug has already been proven sufficiently safe in preclinical models and humans.[21] Drug repurposing could be performed by using various computational or experimental approaches.

This study combines structure-based computational and experimental approaches to identify new antimalarial drugs among FDA-approved drugs targeting *Plasmodium* SHMTs. A molecular docking method was used to screen potential new potent antimalarial drugs from the Drugbank database[22] against *P. vivax* SHMT (*Pv*SHMT) and *P. falciparum* SHMT (*Pf*SHMT). Then, the inhibitory activities of the hit compounds against *Pf*SHMT were investigated by using an enzyme-based inhibition assay. Finally, structural dynamics and mode of action of the most potent compound were studied using 500 ns all-atom molecular dynamics (MD) simulations. The experimental data and atomic details of the new potent *Plasmodium* SHMT inhibitors could facilitate future antimalarial drug discovery.

2. METHODS

2.1. *Plasmodium* SHMT Structures. This study investigated seven *P. vivax* (*Pv*) and *P. falciparum* (*Pf*) SHMT structures. Five crystal structures from seven *Pv*SHMT and *Pf*SHMT complexes were retrieved from the Protein Data Bank (PDB): *Pf*SHMT/PLP (PDB: 4O6Z),[23] *Pv*SHMT/L-Ser Schiff base (PLS; PDB: 4PFN),[15] *Pv*SHMT/D-Ser/folinic acid (PDB: 4OYT),[15] *Pv*SHMT/Gly/pyrazolopyran(+)-85 (PDB: 5GVN),[13] and *Pv*SHMT/Gly/pyrazolopyran(+)-86 (PDB: 5YFZ).[17] The other two structures, 5YFZ/PLS[17] and 4O6Z/PLS[23]/pyrazolopyran(+)-86, were averaged from the final 100 ns of MD simulations in our previous study.[24] Only two subunit chains were selected for further study (chains C and D for *Pf*SHMT and chains A and B for *Pv*SHMT), representing a native *Plasmodium* SHMTs homodimer.[13,15,23]

2.2. Structure-Based Virtual Screening. The 2509 FDA-approved drugs from the Drugbank database[22] were virtually screened to identify those with the potential to be repurposed as antimalarial treatments using a molecular docking method in the AutoDock VinaXB program.[25] The docking study was validated by redocking all ligands (folinic acid, pyrazolopyran-(+)-85, and pyrazolopyran(+)-86) into the substrate-binding cleft (loops 1 to 5)[15,23] of the five *Plasmodium* SHMT crystal structures retrieved from the PDB and two structures from prior MD simulations. A 50 × 50 × 50 Å cubic grid box was created to cover the representative chain (chain A for *Pv*SHMT and chain C for *Pf*SHMT). The molecular docking was performed with 20 docking poses for each compound. Then, the docking scores were ranked from low to high, and the pose with the lowest docking score was selected for further analysis. The molecular docking method results were visualized using Discovery Studio Visualizer 2021[26] and UCSF Chimera version 1.16.[27]

2.3. Preparation and Activity Assay for *Pf*SHMT. *Pf*SHMT was prepared as previously described[28,29] with slight modification. Briefly, the pET100/D-*pfshmt* overexpression vector was used to produce recombinant *Pf*SHMT with an N-terminal six-histidine tag in *Escherichia coli* BL21 (DE3) cells at 16 °C in a ZY autoinduction medium system. Unless otherwise specified, *Pf*SHMT purification was conducted at 4 °C. The cell paste harboring recombinant *Pf*SHMT was resuspended in buffer A (50 mM 4-[2-hydroxyethyl]-1-piperazineethanesulfonic acid [HEPES; pH 7.45], 200 mM, NaCl, and 10% glycerol) containing 10 mM imidazole, 10 μM PLP, and 100 μM phenylmethylsulfonyl fluoride (PMSF), and then lysed by ultrasonication. Next, the crude extract obtained after three rounds of centrifugations at 35,000*g* for 60 min was purified to homogeneity by affinity chromatography using a Nickel-chelating Sepharose column pre-equilibrated with buffer A containing 10 mM imidazole. Then, the column was sequentially washed with buffer A containing 10- and 100

https://doi.org/10.1021/acsomega.3c01309
ACS Omega 2023, 8, 35580−35591

mM imidazole. The column was eluted with buffer A containing a linear gradient of 100−300 mM imidazole. Fractions containing *Pf*SHMT were pooled, and excess PLP was added before concentrating via an ultrafiltration technique. Next, the concentrated enzyme solution was exchanged into buffer B (50 mM HEPES, pH 7.45 containing 1 mM dithiothreitol [DTT], and 0.5 mM ethylenediaminetetraacetic acid [EDTA]) by gel-filtration chromatography using a Sephadex G-25 column. The collected eluent was concentrated by ultrafiltration before a 2-fold excess of PLP was added. Finally, all eluents were stored at −80 °C until needed.

The *Pf*SHMT activity was measured at 25 °C using an enzyme-coupled assay method using $NADP^+$-dependent 5,10-methylenetetrahydrofolate dehydrogenase (MTHFD) as a coupling enzyme.[29] The typical assay reaction was conducted in buffer C (50 mM HEPES, pH 7.5, containing 1 mM DTT, and 0.5 mM EDTA) containing 0.2 mM THF, 3 mM L-Ser, 0.25 mM $NADP^+$, 10 μM MTHFD, and 1 μM *Pf*SHMT. The assay reaction was monitored for $NADP^+$ reduction to NADPH at 375 nm, and one unit of SHMT activity was defined as 1 μmol of NADPH produced per min at pH 7.5 and 25 °C.

2.4. *Pf*SHMT Inhibitor Screening. Eight candidate compounds identified by molecular docking were examined for their ability to inhibit *Pf*SHMT activity: amphotericin B, dihydroergocristine mesylate, rifabutin, rifaximin, nystatin, tubocurarine, digitoxin, and digoxin. The enzyme inhibition assays were performed similarly to the enzyme activity assay described above, except that 100 μM of each compound was added to the reaction. The initial rate of each reaction was measured and compared with the control reaction. Note that the concentration of dimethyl sulfoxide (DMSO; the solvent used to solubilize compounds) in all inhibition assays was fixed at 1% (v/v), which did not affect *Pf*SHMT activity within 3 h (Figure S1).

2.5. Determination of Half Maximal Inhibitory Concentrations (IC_{50}) for *Pf*SHMT Inhibitors. The inhibition assay screening indicated that dihydroergocristine mesylate, digoxin, rifabutin, and amphotericin B could inhibit 20 to 50% of *Pf*SHMT activity. Unfortunately, all these compounds, except amphotericin B, were insoluble in the assay reaction at a concentration of >100 μM. Therefore, only amphotericin B was further analyzed determining of the IC_{50} value.

The *Pf*SHMT activity was measured at various amphotericin B concentrations (20, 50, 100, 120, 150, and 172 μM) and compared with the control reaction. It should be noted that there was no significant difference in the *Pf*SHMT activity between amphotericin B concentrations of 150 and 172 μM. Therefore, 172 μM was used as a final concentration of amphotericin B, rather than 175 or 200 μM. The remaining activity of each reaction was determined and plotted against the amphotericin B concentration added to the reaction. The IC_{50} value was estimated by fitting the curve with the equation ($[Y = \text{bottom} + (\text{top} - \text{bottom})/(1 + 10\hat{}((\text{LogIC}_{50} - X) \times \text{HillSlope}))]$) in GraphPad Prism 7.0 using a symmetrical sigmoidal distribution with variable slope (four-parameter dose−response fit), where the top and bottom values represent the constraint values (upper and lower limits), and X denotes the amphotericin B concentration.

2.6. Kinetics of *Pf*SHMT Inhibition by Amphotericin B. Various amphotericin B concentrations (20 to 172 μM) were added to the enzyme assay reaction to determine the kinetics of *Pf*SHMT inhibition by amphotericin B. The initial rates were measured at different amphotericin B concentrations using varying concentrations of one substrate (L-Ser [0.1 to 6.4 mM] or THF [0.005 to 0.2 mM]) and a fixed concentration of another substrate (L-Ser [3 mM] or THF [0.2 mM]). The double reciprocal plots of initial rates and substrates at different inhibitor concentrations were analyzed using eqs 1 and 2 for competitive and noncompetitive inhibitions, respectively, where v and V represent the initial and maximum velocities, A and I are the substrate and inhibitor concentrations, respectively, K_A is the Michaelis constant for substrate, and K_{is} and K_{ii} are the inhibition constants obtained from the secondary slope and intercept plots, respectively, versus the inhibitor concentration.[30]

$$v = \frac{VA}{K_A\left(1 + {}^{I}/_{K_{is}}\right) + A} \tag{1}$$

$$v = \frac{VA}{K_A\left(1 + {}^{I}/_{K_{is}}\right) + A\left(1 + {}^{I}/_{K_{ii}}\right)} \tag{2}$$

2.7. Preparation of SHMT Structures for MD Simulation. Based on the enzyme inhibition assay, the *Pf*SHMT crystal structure (PDB: 4O6Z)[23] was selected as the protein target for MD simulations. Then, amphotericin B, the hit compound with the lowest IC_{50} value, was superimposed onto chain D, and PLS from *Pv*SHMT/PLS (PDB: 4PFN)[15] was superimposed onto both chains using the UCFS Chimera 1.16 program.[27] According to the standard procedure,[24,31,32] the structure and partial atomic charges of PLS in the protonated ketoenamine form[33] and amphotericin B were calculated with HF/6-31G(d) theory level using the Gaussian09 program.[34] The AMBER ff19SB force field[35] in the AMBER20 program[36] was used for the protein, and the generalized AMBER force field version 2 (GAFF2)[37] was applied to ligands using the Antechamber module of the AMBER20 program.[36] The protonation states of all ionizable groups in *Pf*SHMT were predicted at pH 7.0 using the PROPKA 3.1 program on the PDB 2PQR server.[38] Next, the hydrogen atoms were added to the *Pf*SHMT/PLS/amphotericin B complex based on the water molecules from the crystal structure. The complex was then energy-minimized using 2500 steps of steepest descents (SD) and 2500 steps of the conjugate gradient (CG) method. Then, the minimized structure was solvated by a 12 Å space cutoff of a truncated octahedral TIP3P water box and neutralized by the addition of Na^+ ions. The solvated system was then energy-minimized by the same SD and CG methods as above with a force constant of 50.0 kcal/mol/Å^2 to restrain the protein's heavy atoms. Finally, the whole complex was minimized without a forced constraint to relax the structure before performing MD simulations.

2.8. MD Simulation and Analysis. Based on our previous report,[24] the potent SHMT inhibitors pyrazolopyran(+)-85 and pyrazolopyran(+)-86 were first examined with *Pv*SHMT and *Pf*SHMT using 500 ns MD simulations with the AMBER16 program.[39] Then, 500 ns MD simulations of the chosen ligand (amphotericin B) with the *Pf*SHMT/PLS complex were performed in triplicate using the AMBER20 program.[36] The system was treated using the SHAKE algorithm[40,41] under a periodic boundary condition and a 12 Å distance cutoff for nonbonded interactions. The system was heated from 10.0 to 298.15 K for 100 ps and then equilibrated

https://doi.org/10.1021/acsomega.3c01309
ACS Omega 2023, 8, 35580−35591

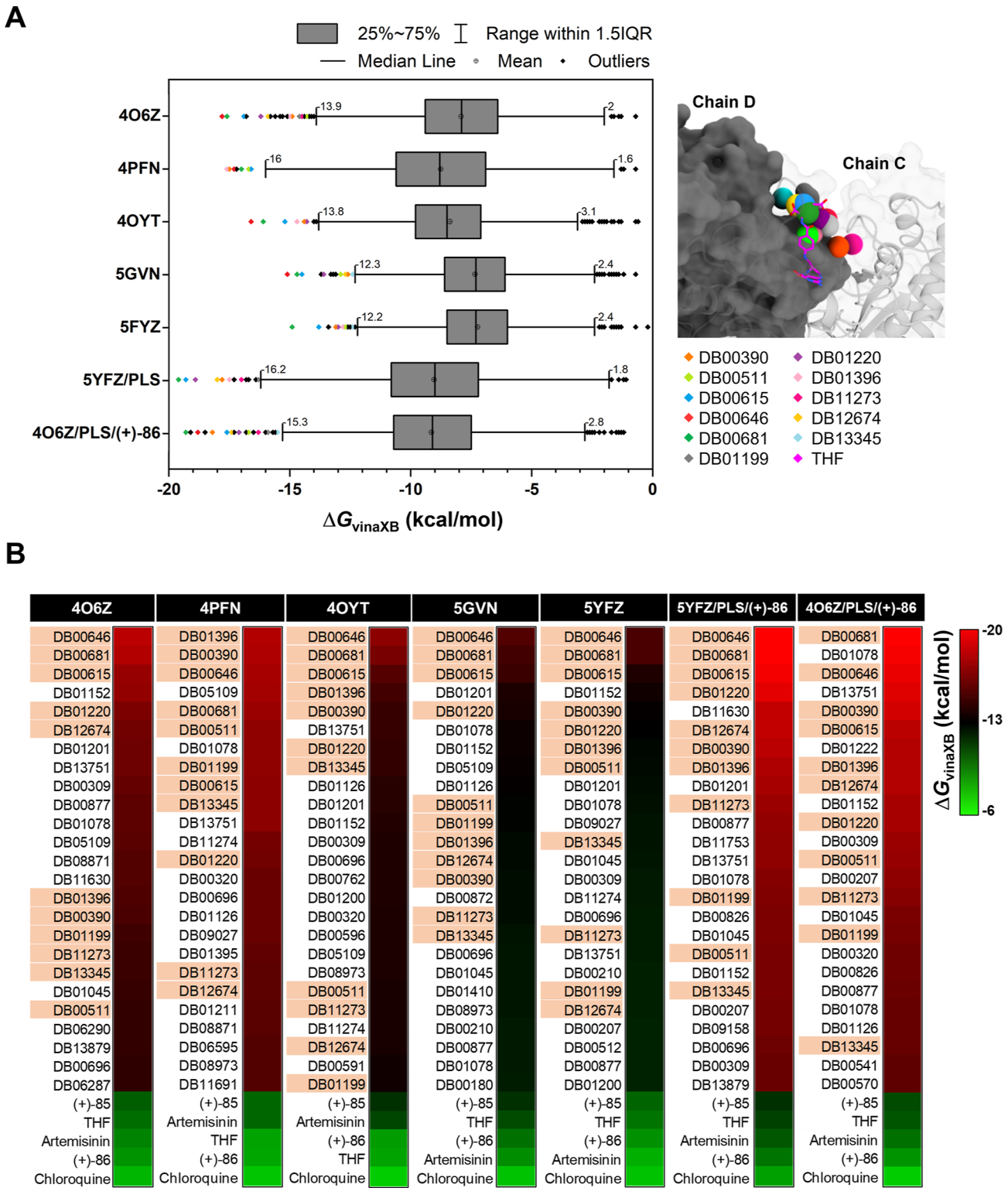

Figure 2. (A) Binding energy (ΔG_{vinaXB}) of the 2509 FDA-approved drugs[22] interacting with *Pv*SHMT and *Pf*SHMT complexes. The inset in A compares the centroids of 11 hit compounds to THF in the *Pf*SHMT binding pocket (PDB: 4O6Z).[23] (B) A heatmap visualization of the 25 hit compounds with the lowest ΔG_{vinaXB} in the *Pv*SHMT and *Pf*SHMT complexes. The names of the 11 potent compounds found with all seven *Plasmodium* SHMT complexes are highlighted in orange.

at 298.15 K for 100 ps. Then, the production phase was conducted for 500 ns using a 2 fs integration time step and an NPT ensemble with 1 atm pressure and 298.15 K temperature. Finally, MD trajectories were extracted for further structural analyses such as rmsd and RMSF using the CPPTRAJ module[42] of the AMBER20 program.[36] Hydrogen bond interactions, per-residue decomposition free energy ($\Delta G_{bind}^{residue}$), solvated interaction energies (ΔG_{SIE}),[43,44] and pharmacophore modeling were predicted using the CPPTRAJ module,[42] MMPBSA.py module[45] of the AMBER16 program,[39] sietraj

https://doi.org/10.1021/acsomega.3c01309
ACS Omega 2023, 8, 35580−35591

software,[43,44] and LigandScout 4.4 program,[46] respectively. The DSSP calculations were conducted using the Timeline analysis tool of VMD 1.8.7 program.[47]

3. RESULTS AND DISCUSSION

3.1. Molecular Docking. Drug virtual screening by molecular docking method was used to screen the 2509 FDA-approved drugs[22] against *Plasmodium* SHMTs for drug repurposing as antimalarial treatments. This study used the AutoDock VinaXB program[25] to screen the potential *Plasmodium* SHMT inhibitors. The searching and scoring functions were set according to the available force field of the AutoDock VinaXB program.[25] The distance, angle, bond, and atom type were mapped to the program library and used to predict the compound's binding energy. The docking results presented in Figure 2A show that most compounds had a binding energy (ΔG_{vinaXB}) of −6 to −11 kcal/mol and docked at the same position in *Pv*SHMT/PLS and *Pf*SHMT/PLS complexes due to their high similarity in 3D protein structure and high amino acid sequence identity in the binding pocket (see Plasmodium SHMT Structures in the above section). In addition, compounds with scores differing significantly from those of others in each complex were defined as outliers. Then, the more negative outliers were ranked by their ΔG_{vinaXB}. The top 25 lowest ΔG_{vinaXB} values (−12 to −19 kcal/mol) of each SHMT complex were chosen for visualization in Figure 2B. Eleven of the top 25 hit compounds were identified with all seven SHMT structures: digoxin (DB00390), acetyldigitoxin (DB00511), rifabutin (DB00615), nystatin (DB00646), amphotericin B (DB00681), tubocurarine (DB01199), rifaximin (DB01220), digitoxin (DB01396), dihydroergocornine (DB11273), lurbinectedin (DB12674), and dihydroergocristine (DB13345). The molecular weights (MW) of the considered compounds were 560 to 920 g/mol (Table S1), almost twice that of THF (445.4292 g/mol[22]). However, the 11 molecules' centroid positions were near that of THF in the *Pf*SHMT binding pocket (Figure 2A, inset) and other crystal ligands; pyrazolopyran(+)-85 and (+)-86 (Figure S2). In addition, their ΔG_{vinaXB} values were less than those of the reference compounds: pyrazolopyran-based inhibitors, THF, and antimalarial drugs. Moreover, many regions of their structures comprised hydroxy groups (Table S1). Therefore, their binding affinities could be greater than those of other compounds in the library. However, due to cost and time limitations, only eight compounds in Table 1 were selected for further investigation in a *Plasmodium* SHMT inhibition assay: digoxin, rifabutin, nystatin, amphotericin B, tubocurarine, rifaximin, digitoxin, and dihydroergocristine. It is worth noting that the docking study revealed a preference for these eight candidate drugs binding to *Pf*SHMT rather than human cytosolic SHMT (*hc*SHMT), with nystatin and amphotericin B presenting particularly strong affinity (Figure S3).

3.2. *Pf*SHMT Inhibitor Screening. The *Pf*SHMT inhibiting activities of the eight candidate compounds identified by molecular docking (amphotericin B, dihydroergocristine mesylate, rifabutin, rifaximin, nystatin, tubocurarine, digitoxin, and digoxin) were assessed in enzymatic reaction assays and compared to those in control reaction assays. Note that the concentration of each candidate compound used in the *Pf*SHMT inhibition assay, prepared by diluting a very high concentration stock solution (millimolar scale) in DMSO, was initially 10 μM. However, the *Pf*SHMT activity was unaffected (data not shown). When the concentration was increased to 100 μM, the *Pf*SHMT activity decreased (Figure S4). Therefore, a 100 μM concentration was used in all subsequent assays.

Table 1. Eight Potent Compounds in Drugbank[22] Showing *Pf*SHMT Inhibitory Activity

name	drug activity
digoxin (DB00390)	used to treat mild-to-moderate heart failure used for ventricular response rate control in chronic atrial fibrillation
rifabutin (DB00615)	an antibiotic used to treat Mycobacterium avium complex disease in patients with human immunodeficiency viral infections (HIV)
nystatin (DB00646)	a mixture of antifungal polyenes
amphotericin B (DB00681)	an antifungal used to treat serious fungal infections and leishmaniasis
tubocurarine (DB01199)	a nondepolarizing neuromuscular blocking agent
rifaximin (DB01220)	an antibiotic used to treat gastrointestinal bacterial infections
digitoxin (DB01396)	a cardiac glycoside used to treat congestive cardiac insufficiency, arrhythmias, and heart failure
dihydroergocristine (DB13345)	an ergot alkaloid used to delay progressive mental decline in conditions such as Alzheimer's disease

Figure 3A shows that dihydroergocristine mesylate, digoxin, rifabutin, and amphotericin B inhibited *Pf*SHMT activity by about 20−50% relative to the control reactions, while the remaining compounds did not. Interestingly, all compounds except amphotericin B precipitated in the assay reaction when their concentrations were >100 μM (data not shown). Therefore, only amphotericin B had its IC_{50} value determined.

Since the other compounds had limited solubility only at 100 μM and appeared less capable of inhibiting *Pf*SHMT than amphotericin B, we investigated whether they showed time-course inhibition of *Pf*SHMT activity at 100 μM. Figure S4 shows that, after incubation for 1 to 3 h, rifaximin could inhibit *Pf*SHMT activity up to 60% relative to the control reactions. Similarly, tubocurarine and digitoxin inhibited *Pf*SHMT activity by about 40%, and dihydroergocristine mesylate and rifabutin by about 25% after a 3 h incubation. In contrast, digoxin and nystatin showed no significant inhibition after 3 h incubation. Notably, no precipitation of any compound at 100 μM was observed during the 3 h incubation. These data indicated that rifaximin, tubocurarine, digitoxin, dihydroergocristine mesylate, and rifabutin were slow *Pf*SHMT inhibitors. Interestingly, although nystatin has a chemical structure related to amphotericin B, it did not similarly inhibit *Pf*SHMT at the concentration tested. Differences in their hydroxyl substituent stereoisomerism and number of conjugated dienes may affect their inhibition efficacy.

3.3. IC_{50} Value of Amphotericin B. The screening of *Pf*SHMT inhibitors described above indicated that amphotericin B was a potent *Pf*SHMT inhibitor that could be miscible in the assay reaction. Therefore, we measured the *Pf*SHMT activity at amphotericin B concentrations from 20 to 172 μM to determine its IC_{50}. Figure 3B shows that based on the plot of the percentage remaining activity versus the logarithm of amphotericin B concentration, the IC_{50} value of amphotericin B was 106 ± 1 μM, higher than those of previously reported pyrazolopyran inhibitors (+)-85 (90 ± 4 nM) and (+)-86 (97 ± 1 nM).[13] This difference might reflect the higher MW of amphotericin B (924.079 g/mol) compared to the pyrazolopyran inhibitors (~460 g/mol[22]), which might hinder its binding at the enzyme active site, lowering its inhibition

https://doi.org/10.1021/acsomega.3c01309
ACS Omega 2023, 8, 35580−35591

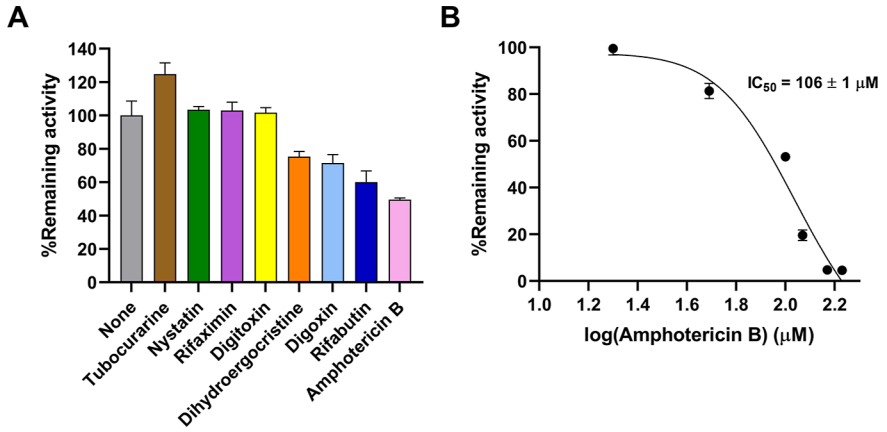

Figure 3. (A) *Pf*SHMT inhibitor screening. *Pf*SHMT activity was measured with 100 μM of each candidate compound (tubocurarine, nystatin, rifaximin, digitoxin, dihydroergocristine mesylate, digoxin, rifabutin, and amphotericin B) and compared to the control reaction. (B) Amphotericin B's IC_{50} for inhibiting *Pf*SHMT. *Pf*SHMT activity was measured with different amphotericin B concentrations (20 to 172 μM) and compared to the control reaction. Error bars represent standard deviations (S.D.) from three replicates.

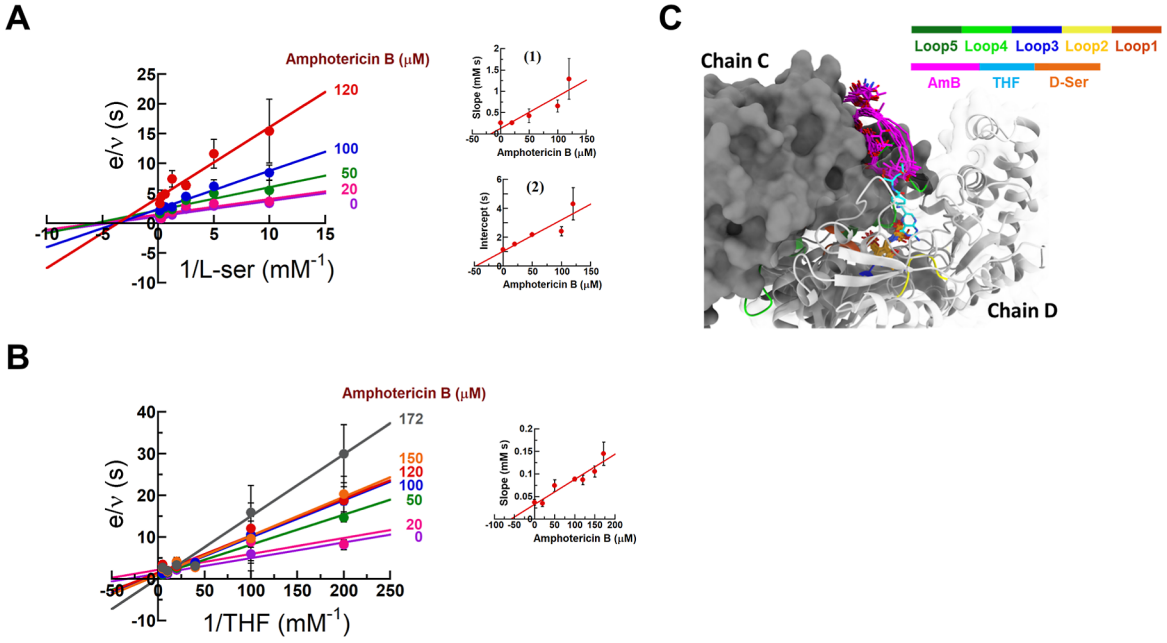

Figure 4. *Pf*SHMT inhibition mechanism by amphotericin B. The double-reciprocal (primary) plots of initial rates with (A) L-Ser and (B) THF substrates and different amphotericin B concentrations (0 to 172 μM). Insets (1) and (2) in (A) show secondary plots of average slopes and intercepts obtained from the primary plot, respectively, versus amphotericin B. The inset in (B) shows the secondary plot of average slopes obtained from the primary plot versus amphotericin B. The estimated inhibition constants obtained from these plots are summarized in Table 2. Error bars represent standard deviations across the three replicates. (C) The position of amphotericin B during the final 100 ns of the MD simulation compared to the THF substrate in the *Pf*SHMT binding pocket.

efficacy. In addition, different DMSO percentages used could cause differences in the enzyme inhibition. While 1% DMSO was used in this study, 5% DMSO was used in the pyrazolopyran inhibitory assays.[13]

3.4. Amphotericin B Inhibition Mechanism. The inhibition kinetics of amphotericin B toward *Pf*SHMT reactions were characterized to describe the inhibition mechanism of amphotericin B. Figure 4 shows the double-reciprocal (primary) plots of e/v versus either L-Ser (Figure 4A) or THF (Figure 4B) at different amphotericin B concentrations, which can be used to characterize the inhibition mechanism type. The primary plot of e/v versus L-Ser concentration with increasing amphotericin B concentrations (Figure 4A) showed converging lines that intersected the left side of the Y-axis, indicating a noncompetitive inhibition mechanism. Based on the primary plot, two inhibition constants, K_{is} and K_{ii}, could be determined from the secondary plots of the averages of primary slopes (Figure 4A, inset 1) and intercepts (Figure 4A, inset 2) versus amphotericin B, respectively, which were estimated on the abscissa axis as 18 and 48 μM, respectively (Table 2). In contrast, the primary plot of e/v versus THF concentration with increasing amphotericin B concentrations (Figure 4B) showed intersecting lines on the Y-axis, indicating a competitive inhibition mechanism. The secondary plot of primary slopes versus amphotericin B (Figure 4B, inset) provided a K_{is} estimate of 59 μM (Table 2). Based on the amphotericin B structure, it could be inferred that amphoter-

https://doi.org/10.1021/acsomega.3c01309
ACS Omega 2023, 8, 35580−35591

Table 2. Estimated Inhibition Constants for Amphotericin B with *Pf*SHMT[a]

substrate	amphotericin B (μM)		inhibition type
	K_{is}	K_{ii}	
l-Ser	18	48	noncompetitive
THF	59	ND	competitive

[a]ND, not determined.

icin B competes with THF binding at the active site but is noncompetitive with the L-Ser substrate (Figure 4C). The data suggest that amphotericin B might be a promising *Pf*SHMT inhibitor.

The AutoDock VinaXB program's genetic algorithm[48] predicted amphotericin B's binding pocket was above the THF binding pocket of *Plasmodium* SHMT. However, some regions of the THF binding pocket (loop 4) showed an interaction with amphotericin B (Figure 4C). This binding position of amphotericin B might interfere with the THF binding in the *Plasmodium* SHMT binding pocket. The 500 ns MD simulations of the *Pf*SHMT/PLS/amphotericin B complex showed the stability of amphotericin B in its binding site. The 10 snapshots from the last 100 ns of the MD simulation showed a similar amphotericin B position on the *Pf*SHMT surface (Figure 4C). This position could be referred to as the correct amphotericin B binding site on *Plasmodium* SHMT and was consistent with the site predicted by the AutoDock VinaXB program.[25]

3.5. *Plasmodium* SHMT Complex Stability. The root-mean-square deviation (rmsd) for the protein backbone atoms

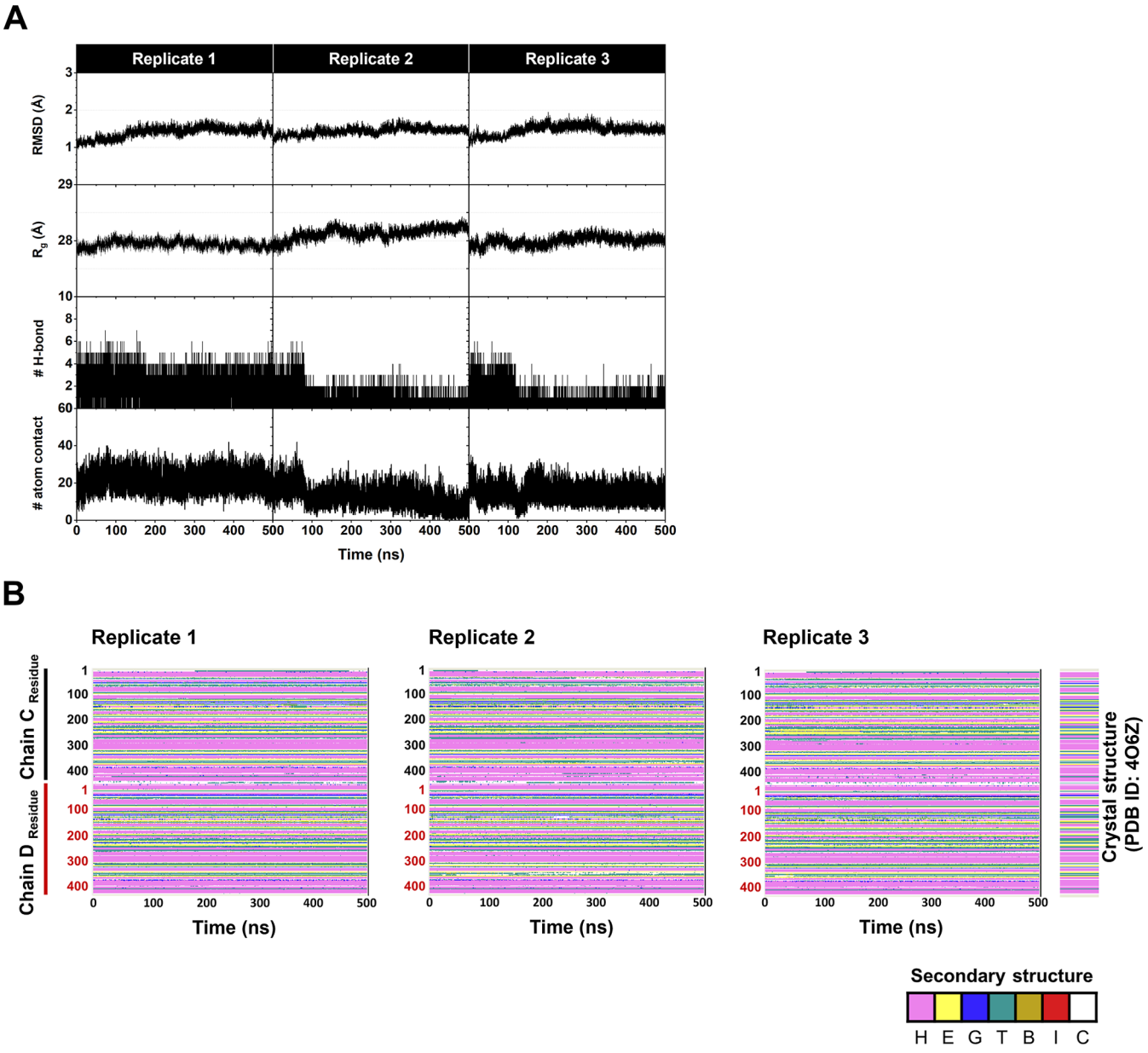

Figure 5. (A) Backbone rmsd, R_g, # H-bonds, and #atom contacts of the *Pf*SHMT/PLS/amphotericin B complex in three replicate 500 ns MD simulations. (B) DSSP analysis of *Pf*SHMT chains C and D, showing secondary structure elements: α-helix (H), extended conformation (E), 3−10 helix (G), turn (T), β-bridge (B), π-helix (I), and random coils (C). Pink, yellow, blue, green, goldenrod, red, and white shading represent these respective secondary structure elements.

https://doi.org/10.1021/acsomega.3c01309
ACS Omega 2023, 8, 35580−35591

(i.e., N, C, O, and Cα) of *Pf*SHMT/PLS bound to amphotericin B was calculated along the 500 ns MD simulation to determine the complex stability in an aqueous solution. The backbone rmsd of the *Pf*SHMT/PLS/amphotericin B complex (Figure 5A, top) slowly increased (until ∼200, ∼ 100, and ∼200 ns in replicates 1 to 3, respectively) and then fluctuated slightly by approximately 1.5 ± 0.1 Å across three replicates. The secondary structure annotations provided by DSSP calculation can be used to study protein folding, stability, and other structural properties along the simulations. Figure 5B presents the DSSP analysis, which reveals that the complex under consideration exhibited exceptional stability throughout the simulation when compared to the crystal structure of *Pf*SHMT with a covalently bound PLP Schiff-base (4O6Z.pdb).[23] This finding suggests that all systems reached a state of equilibrium. Furthermore, a comprehensive assessment of the system's conformational stability was conducted using additional parameters, including the radius of gyration (R_g), number of intermolecular hydrogen bonds (#H-bond), and number of atom contacts (#atom contact). Replication one, depicted in Figure 5A, exhibited a notable R_g value of 27.9 ± 0.1 Å, a significant number of intermolecular hydrogen bonds (2 ± 1), and a substantial number of atom contacts (21 ± 4) in the last 100 ns. These findings substantiate the strong interaction between amphotericin B and *Pf*SHMT in replication one when compared to replication two and three, which displayed R_g values of 28.2 ± 0.1 and 28.0 ± 0.1 Å, #H-bond values of 1 ± 1 and 1 ± 1, and #atom contact values of 8 ± 4 and 14 ± 4, respectively. Therefore, replicate one was selected as the representative system for the subsequent analysis. Note that other investigations of the representative chain showed a greater binding interaction with *Pf*SHMT.

3.6. Amphotericin B Binding Affinity. Solvated interaction energies (ΔG_{SIE}) were calculated to amphotericin B binding affinity[43,44] for the *Pf*SHMT/PLS complex. This calculation used 100 snapshots extracted from the last 100 ns of the representative replicate's MD simulation. Table 3 shows that the electrostatic energy (ΔE_{ele}) plays a more important role in the molecular complexation of *Pf*SHMT/PLS/amphotericin B (−55.31 ± 0.98 kcal/mol) than van der Waals interactions (ΔE_{vdW}; −46.74 ± 0.44 kcal/mol). In contrast, with pyrazolopyran-based inhibitors, which bind at the same site as THF substrate on *Plasmodium* SHMT, the ΔE_{vdW} was a major driving force[24] in *Plasmodium* SHMT/PLS/pyrazolopyran−inhibitor complex formation. This difference in the binding site resulted in the different main forces driving the complexation of *Plasmodium* SHMT with amphotericin B and pyrazolopyran-based inhibitors. In summary, while the ΔG_{exp} of amphotericin B was not as good as that of pyrazolopyran(+)-86,[13] its computationally predicted ΔG_{SIE} suggested that it had a good binding affinity for the ligand-binding pocket of *Plasmodium* SHMT.

Table 3. Solvated Interaction Energies (ΔG_{SIE}) and Its Components for *Pf*SHMT Complexed with PLS and Amphotericin B[a]

energy component	*Pf*SHMT/PLS/amphotericin B (kcal/mol)
ΔE_{vdW}	−46.74 ± 0.44
ΔE_{ele}	−55.31 ± 0.98
γ ΔMSA	−9.17 ± 0.11
ΔG_{bind}^{R}	32.39 ± 1.03
C	−2.89
α	0.10
ΔG_{SIE}	−11.15 ± 0.09
ΔG_{exp}	−5.42

[a]ΔMSA is the change in the molecular surface area after binding; ΔG_{bind}^{R} is the change in the reaction field energy between free and bound states calculated by solving the Poisson equation;[49,50] α is the global proportionality coefficient reflecting the loss of configurational entropy; γ is the molecular area coefficient; C is a constant value; ΔG_{exp} is calculated from the IC_{50} using the equation $\Delta G_{exp} \approx -RT \ln(IC_{50})$, where R is the universal gas constant (1.987×10^{-3} kcal/mol/K), and T is the temperature in K.

To predict the interaction between amphotericin B and residues around the binding site on *Plasmodium* SHMT, a $\Delta G_{bind}^{residue}$ was calculated for each residue based on the molecular mechanics with the generalized Born and surface area solvation method. Figure 6A shows that there were 13 key residues with a $\Delta G_{bind}^{residue}$ less than −0.5 kcal/mol: Y58, P59, Y63, Y78, G93, N95, F249, K251, N262, Q259, F266, P267, and V365. Most of these key residues were not reported to have an important role in ligand binding. However, N262 had the lowest ($\Delta G_{bind}^{residue}$) with amphotericin B of −6.03 kcal/mol. K251, the residue in the short loop of *Pf*SHMT associated with the flap motif of human SHMT,[23] strongly interacted with amphotericin B ($\Delta G_{bind}^{residue}$ of −3.15 kcal/mol). Moreover, Y63, F266, and V365, key stabilizing residues for THF and the pyrazolopyran inhibitors,[17,23,24] had ($\Delta G_{bind}^{residue}$ of −0.73, −2.68, and −0.67 kcal/mol, respectively). The key residues Y58, P59, Y78, G93, N95, F249, Q259, and P267 had ($\Delta G_{bind}^{residue}$ values of −2.97, −0.61, −1.94, −0.90, −0.55, −0.64, −1.50, and −1.60 kcal/mol, respectively). However, C364 showed an unfavorable interaction with amphotericin B ($\Delta G_{bind}^{residue}$ of 0.70 kcal/mol). These predictions identified 13 critical pocket residues in *Pf*SHMT and other binding residues (Figure 6B), which differ noticeably from the key stabilizing residues of THF and the pyrazolopyran-based inhibitors. These data could be supportive information for novel inhibitor development targeting *Plasmodium* SHMT.

3.7. Key Residues around the Amphotericin B Binding Site. Key residues around the amphotericin B binding site of *Pf*SHMT were identified by pharmacophore modeling. Pharmacophore modeling is a computational method for discovering intermolecular interactions of active compounds with a specific biological target comprising the H-bond donor, H-bond acceptor, hydrophobic interaction, and positive and negative ionizable groups.[51,52] This study used 10,000 snapshots from the final 100 ns of MD simulations of *Pf*SHMT/PLS/amphotericin B as a template to create a structure-based pharmacophore model. The 2D and 3D in Figure 7A indicate the *Pf*SHMT/PLS/amphotericin B complex critical pharmacophore features were hydrophobic interactions, H-bond contacts, and negative ionizable groups. Y63 and V365 in *Pf*SHMT formed hydrophobic interactions with amphotericin B. Y78, E90, K251, D258, N262, and F266 formed H-bond contacts with amphotericin B. Y63, F266, and V365 were also previously reported as key residues in interactions with the pyrazolopyran-based inhibitors.[15,17,23,24] The protein−ligand interaction fingerprint conducted with the PLIP web tool[53] provides further support for the pharmacophore modeling results. The analysis highlights the critical involvement of specific residues, such as K61, Y78, E90, K251, D258, N262, F266, and P267, in ligand binding (see Figure S5). Additionally, the map of interactions with ≥20% occurrences (Figure S6) also suggested high appearance and

https://doi.org/10.1021/acsomega.3c01309
ACS Omega 2023, 8, 35580−35591

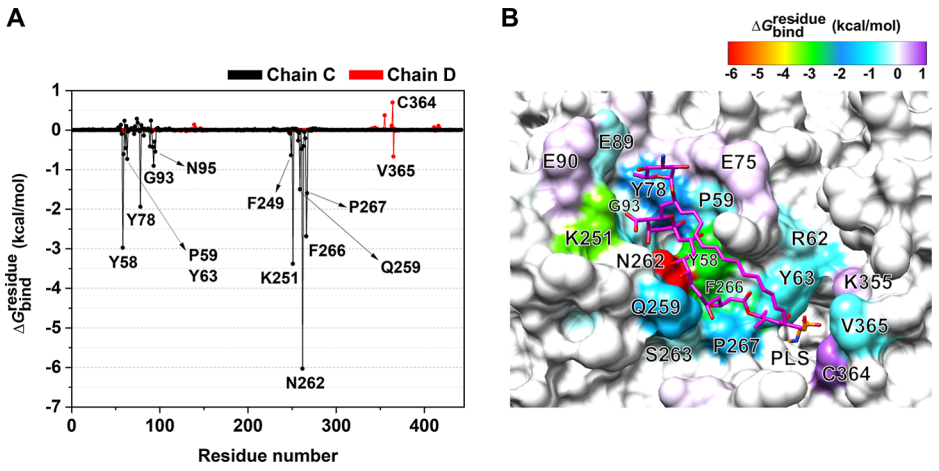

Figure 6. (A) $\Delta G_{bind}^{residue}$ of the *Pf*SHMT/PLS/amphotericin B complex on the representative chain with an energy cutoff of ±0.5 kcal/mol. (B) The key *Pf*SHMT residues involved in amphotericin B binding, colored according to their $\Delta G_{bind}^{residue}$.

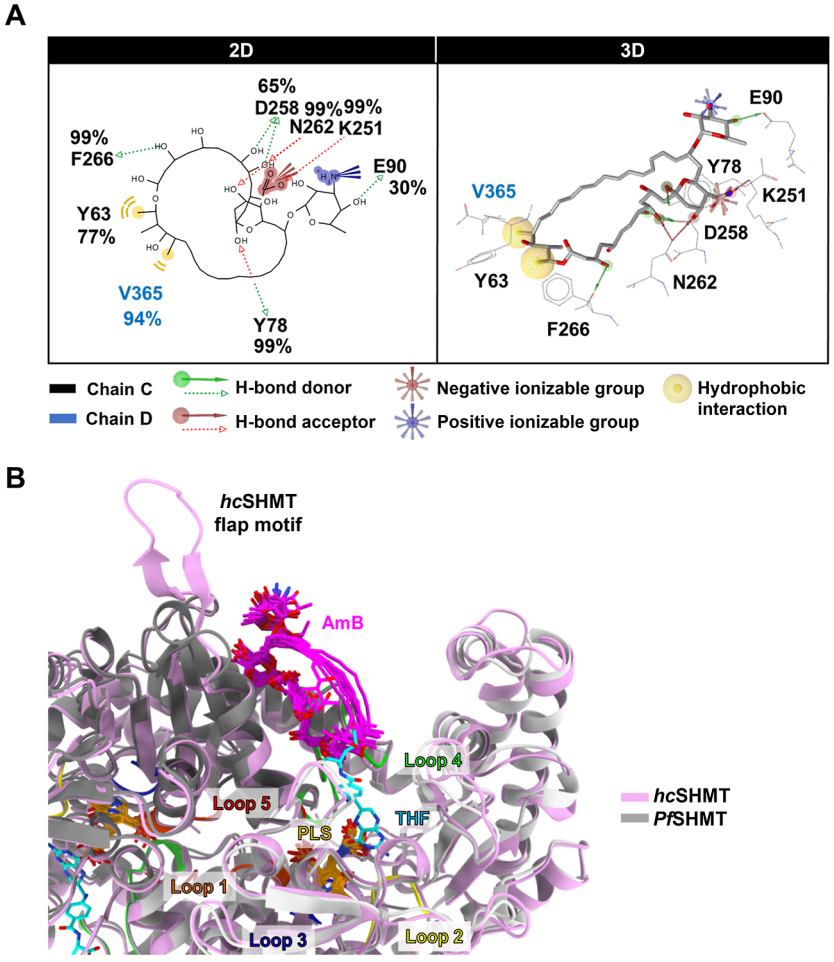

Figure 7. (A) 2D and 3D pharmacophore models for *Pf*SHMT/PLS/amphotericin B based on the final 100 ns of the MD simulation. Note that percentage occurrences of ≥20% are indicated in the 2D representation. (B) The overlaid structures of *Pf*SHMT/PLS/amphotericin B and *hc*SHMT with an rmsd of 0.705 Å. The ten amphotericin B conformations in the binding site were extracted from the final 100 ns of the MD simulation.

occurrence percentages (≥80%) for interactions between *Pf*SHMT residues and amphotericin B, including Y78, K251, N262, F266, and V365. V365 showed a hydrophobic interaction with amphotericin B with 94% appearance and occurrence. Strong H-bond interactions were observed for K251, N262, and F266 (99% appearance and occurrence). Regarding the negative interaction group, only K251 showed a 99% occurrence in *Pf*SHMT. The RMSF and *B*-factor analyses of *Pf*SHMT (Figure S7) illustrated the overall stability of the ligand binding site. These obtained results indicate the preferable environment of the *Pf*SHMT/PLS complex for amphotericin B.

https://doi.org/10.1021/acsomega.3c01309
ACS Omega 2023, 8, 35580−35591

The overlaid human cytosolic SHMT (*hc*SHMT)[54] and *Pf*SHMT structures showed similar conformations, with an rmsd of 0.705 Å (Figure 7B). However, the main region of the flap motif differed between *hc*SHMT and *Pf*SHMT. The flap motif, a unique β-hairpin structure in *hc*SHMT comprising 13 amino acids (273-VKSVDPKTGKEIL-285), was located on top of the THF binding site.[55] This region is found only in mammalian cytosolic SHMTs. However, the superimposition of these two structures showed that the *Pf*SHMT THF binding pocket was not involved in the *hc*SHMT flap motif. K251 in *Pf*SHMT, a key residue for amphotericin B binding, was identified as one residue in a short loop related to the *hc*SHMT flap motif.[23] The interaction of amphotericin B with *Pf*SHMT involves many residues (as mentioned in the Amphotericin B Binding Affinity section). Therefore, only K251 might not affect the interaction of amphotericin B with *Pf*SHMT.

4. CONCLUSIONS

The screening of 2509 FDA-approved drugs on *Plasmodium* SHMT targets by molecular docking using the AutoDock VinaXB program revealed that 11 hit compounds with 4 to 10 kcal/mol lower binding energies (ΔG_{vinaXB}) than the known SHMT inhibitor pyrazolopyran(+)-86 and antimalarial drugs artemisinin and chloroquine across all seven complexes. However, only eight compounds (digoxin, rifabutin, nystatin, amphotericin B, tubocurarine, rifaximin, digitoxin, and dihydroergocristine) were investigated further in the *Plasmodium* SHMT inhibition assay. The experimental results suggested that amphotericin B was the best inhibitor, with the lowest IC_{50} of 106 ± 1 μM. Moreover, inhibition mechanism studies indicated that amphotericin B could be a promising competitive inhibitor with THF for *Pf*SHMT. To clarify the binding affinity and mode of action of *Pf*SHMT/PLS/amphotericin B, we performed 500 ns MD simulations. The backbone rmsd suggested that the *Pf*SHMT/PLS/amphotericin B complex had high conformational stability throughout the 500 ns simulations. However, the R_g, #H-bonds, and #atom contacts within the enzyme active site indicated higher complex stability and a more favorable binding interaction in the replicate one, which was used for further investigations. The solvated interaction energy (ΔG_{SIE}) prediction based on 100 snapshots from the last 100 ns of the MD simulations exhibited a preferable interaction between amphotericin B and the *Pf*SHMT/PLS complex with a ΔG_{exp} almost 2-folds, higher than pyrazolopyran(+)-86. The pharmacophore modeling and interaction map indicated that Y78, K151, N262, F266, and V365 were essential binding residues for amphotericin B. Moreover, the molecular docking results confirmed that eight identified drugs specifically interacted with *Pf*SHMT rather than *hc*SHMT. Our findings identify a new inhibitor against *Plasmodium* SHMTs, an FDA-approved drug with known activity. Our experimental and computational results provide a potential new core structure for future drug development that differs from currently known SHMT inhibitors.

■ ASSOCIATED CONTENT

Supporting Information

The Supporting Information is available free of charge at https://pubs.acs.org/doi/10.1021/acsomega.3c01309.

Time-dependent activity of *Pf*SHMT; hit drugs information; interaction heatmap of *Pf*SHMT/PLS/amphotericin B complex; and docking score of hit drugs on *Pf*SHMT and *hc*SHMT (PDF)

■ AUTHOR INFORMATION

Corresponding Author

Thanyada Rungrotmongkol − *Program in Bioinformatics and Computational Biology, Graduate School, Chulalongkorn University, Bangkok 10330, Thailand; Center of Excellence in Biocatalyst and Sustainable Biotechnology, Department of Biochemistry, Faculty of Science, Chulalongkorn University, Bangkok 10330, Thailand;* orcid.org/0000-0002-7402-3235; Phone: +66-2218-5426; Email: thanyada.r@chula.ac.th; Fax: +66-2218-5418

Authors

Pitchayathida Mee-udorn − *Program in Bioinformatics and Computational Biology, Graduate School, Chulalongkorn University, Bangkok 10330, Thailand;* orcid.org/0000-0002-3351-5911

Kochakorn Phiwkaow − *Department of Biochemistry, Faculty of Science, Burapha University, Chonburi 20131, Thailand*

Ruchanok Tinikul − *Department of Biochemistry and Center for Excellence in Protein and Enzyme Technology, Faculty of Science, Mahidol University, Bangkok 10400, Thailand*

Kamonpan Sanachai − *Department of Biochemistry, Faculty of Science, Khon Kaen University, Khon Kaen 40002, Thailand;* orcid.org/0000-0003-2605-5360

Somchart Maenpuen − *Department of Biochemistry, Faculty of Science, Burapha University, Chonburi 20131, Thailand*

Complete contact information is available at: https://pubs.acs.org/10.1021/acsomega.3c01309

Notes

The authors declare no competing financial interest.

■ ACKNOWLEDGMENTS

This work was supported by the 90th Anniversary of Chulalongkorn University Fund (Ratchadaphiseksomphot Endowment Fund) under Grant GCUGR1125641004D-004 (to P.M.); Science Achievement Scholarship of Thailand (to P.M.); the National Research Council of Thailand (NRCT) under Grant NRCT5-RSA63012-01 (to S.M.); and the Office of the Permanent Secretary, Ministry of Higher Education, Science, Research and Innovation under Grant RGNS 63-179 (to R.T.). We also thank the Program in Bioinformatics and Computational Biology, Graduate School and Faculty of Science, Chulalongkorn University (to P.M. and T.R.); Faculty of Science, Burapha University (to S.M. and K.P.); and the Center for Excellence in Protein and Enzyme Technology (CPET), Faculty of Science, Mahidol University (to R.T.).

■ REFERENCES

(1) Amir, A.; Russell, B.; Liew, J. W. K.; Moon, R. W.; Fong, M. Y.; Vythilingam, I.; Subramaniam, V.; Snounou, G.; Lau, Y. L. Invasion characteristics of a *Plasmodium knowlesi* line newly isolated from a human. *Sci. Rep.* **2016**, *6*, 24623.

(2) Groger, M.; Fischer, H. S.; Veletzky, L.; Lalremruata, A.; Ramharter, M. A systematic review of the clinical presentation, treatment and relapse characteristics of human *Plasmodium ovale* malaria. *Malar. J.* **2017**, *16*, 112.

(3) Maeno, Y.; Quang, N. T.; Culleton, R.; Kawai, S.; Masuda, G.; Nakazawa, S.; Marchand, R. P. Humans frequently exposed to a range of non-human primate malaria parasite species through the bites of Anopheles dirus mosquitoes in South-central Vietnam. *Parasites Vectors* **2015**, *8*, 376.
(4) Singh, B.; Daneshvar, C. Human infections and detection of *Plasmodium knowlesi*. *Clin. Microbiol. Rev.* **2013**, *26*, 165−184.
(5) World Health Organization. *International travel and health: situation as on 1 January 2012*; World Health Organization: Geneva, Switzerland, 2012.
(6) Geleta, G.; Ketema, T. Severe malaria associated with *Plasmodium falciparum* and *P. vivax* among children in Pawe Hospital, Northwest Ethiopia. *Malar. Res. Treat.* **2016**, *2016*, 1−7.
(7) World Health Organization. *World Malaria Report 2020*; World Health Organization: Geneva, Switzerland, 2020.
(8) Savarino, A.; Di Trani, L.; Donatelli, I.; Cauda, R.; Cassone, A. New insights into the antiviral effects of chloroquine. *Lancet Infect. Dis.* **2006**, *6*, 67−69.
(9) World Health Organization. *Artemisinin resistance and artemisinin-based combination therapy efficacy: status report*; World Health Organization: Geneva, Switzerland, 2018.
(10) Tantiamornkul, K.; Pumpaibool, T.; Piriyapongsa, J.; Culleton, R.; Lek-Uthai, U. The prevalence of molecular markers of drug resistance in *Plasmodium vivax* from the border regions of Thailand in 2008 and 2014. *Int. J. Parasitol.: Drugs Drug Resist.* **2018**, *8*, 229−237.
(11) Noisang, C.; Prosser, C.; Meyer, W.; Chemoh, W.; Ellis, J.; Sawangjaroen, N.; Lee, R. Molecular detection of drug resistant malaria in Southern Thailand. *Malar. J.* **2019**, *18*, 275.
(12) Locasale, J. W. Serine, glycine and one-carbon units: cancer metabolism in full circle. *Nat. Rev. Cancer* **2013**, *13*, 572−583.
(13) Schwertz, G.; Witschel, M. C.; Rottmann, M.; Bonnert, R.; Leartsakulpanich, U.; Chitnumsub, P.; Jaruwat, A.; Ittarat, W.; Schäfer, A.; Aponte, R. A.; et al. Antimalarial inhibitors targeting serine hydroxymethyltransferase (SHMT) with *in vivo* efficacy and analysis of their binding mode based on X-ray cocrystal structures. *J. Med. Chem.* **2017**, *60*, 4840−4860.
(14) Witschel, M. C.; Rottmann, M.; Schwab, A.; Leartsakulpanich, U.; Chitnumsub, P.; Seet, M.; Tonazzi, S.; Schwertz, G.; Stelzer, F.; Mietzner, T.; et al. Inhibitors of *Plasmodial* serine hydroxymethyltransferase (SHMT): cocrystal structures of pyrazolopyrans with potent blood-and liver-stage activities. *J. Med. Chem.* **2015**, *58*, 3117−3130.
(15) Chitnumsub, P.; Jaruwat, A.; Riangrungroj, P.; Ittarat, W.; Noytanom, K.; Oonanant, W.; Vanichthanankul, J.; Chuankhayan, P.; Maenpuen, S.; Chen, C. J.; et al. Structures of *Plasmodium vivax* serine hydroxymethyltransferase: implications for ligand-binding specificity and functional control. *Acta Crystallogr., Sect. D: Biol. Crystallogr.* **2014**, *70*, 3177−3186.
(16) Mohs, R. C.; Greig, N. H. Drug discovery and development: role of basic biological research. *Alzheimer's Dementia* **2017**, *3*, 651−657.
(17) Schwertz, G.; Witschel, M. C.; Rottmann, M.; Leartsakulpanich, U.; Chitnumsub, P.; Jaruwat, A.; Amornwatcharapong, W.; Ittarat, W.; Schäfer, A.; Aponte, R. A.; et al. Potent inhibitors of *Plasmodial* serine hydroxymethyltransferase (SHMT) featuring a spirocyclic scaffold. *ChemMedChem* **2018**, *13*, 931−943.
(18) Zhang, Z.; Zhou, L.; Xie, N.; Nice, E. C.; Zhang, T.; Cui, Y.; Huang, C. Overcoming cancer therapeutic bottleneck by drug repurposing. *Signal Transduction Targeted Ther.* **2020**, *5*, 113.
(19) Ahmad, S.; Qazi, S.; Raza, K. *Translational Bioinformatics Methods for Drug Discovery and Drug Repurposing*; Academic Press, 2021.
(20) Pushpakom, S.; Iorio, F.; Eyers, P. A.; Escott, K. J.; Hopper, S.; Wells, A.; Doig, A.; Guilliams, T.; Latimer, J.; McNamee, C.; Norris, A.; Sanseau, P.; Cavalla, D.; Pirmohamed, M. Drug repurposing: progress, challenges and recommendations. *Nat. Rev. Drug Discovery* **2019**, *18*, 41−58.
(21) Pillaiyar, T.; Meenakshisundaram, S.; Manickam, M.; Sankaranarayanan, M. A medicinal chemistry perspective of drug repositioning: recent advances and challenges in drug discovery. *Eur. J. Med. Chem.* **2020**, *195*, 112275.
(22) Wishart, D. S.; Feunang, Y. D.; Guo, A. C.; Lo, E. J.; Marcu, A.; Grant, J. R.; Sajed, T.; Johnson, D.; Li, C.; Sayeeda, Z.; et al. DrugBank 5.0: a major update to the DrugBank database for 2018. *Nucleic Acids Res.* **2018**, *46*, D1074−D1082.
(23) Chitnumsub, P.; Ittarat, W.; Jaruwat, A.; Noytanom, K.; Amornwatcharapong, W.; Pornthanakasem, W.; Chaiyen, P.; Yuthavong, Y.; Leartsakulpanich, U. The structure of *Plasmodium falciparum* serine hydroxymethyltransferase reveals a novel redox switch that regulates its activities. *Acta Crystallogr., Sect. D: Biol. Crystallogr.* **2014**, *70*, 1517−1527.
(24) Mee-udorn, P.; Nutho, B.; Chootrakool, R.; Maenpuen, S.; Leartsakulpanich, U.; Chitnumsub, P.; Rungrotmongkol, T. Structural dynamics and in silico design of pyrazolopyran-based inhibitors against *Plasmodium* serine hydroxymethyltransferases. *J. Mol. Liq.* **2022**, *362*, 119737.
(25) Koebel, M. R.; Schmadeke, G.; Posner, R. G.; Sirimulla, S. AutoDock VinaXB: implementation of XBSF, new empirical halogen bond scoring function, into AutoDock Vina. *J. Cheminf.* **2016**, *8*, 27.
(26) BIOVIA, Dassault Systèmes. *The Discovery Studio Visualizer*. v21.1.0; Dassault Systèmes: San Diego, 2021.
(27) Pettersen, E. F.; Goddard, T. D.; Huang, C. C.; Couch, G. S.; Greenblatt, D. M.; Meng, E. C.; Ferrin, T. E. UCSF Chimera−a visualization system for exploratory research and analysis. *J. Comput. Chem.* **2004**, *25*, 1605−1612.
(28) Maenpuen, S.; Sopitthummakhun, K.; Yuthavong, Y.; Chaiyen, P.; Leartsakulpanich, U. Characterization of *Plasmodium falciparum* serine hydroxymethyltransferase−a potential antimalarial target. *Mol. Biochem. Parasitol.* **2009**, *168*, 63−73.
(29) Sopitthummakhun, K.; Thongpanchang, C.; Vilaivan, T.; Yuthavong, Y.; Chaiyen, P.; Leartsakulpanich, U. *Plasmodium* serine hydroxymethyltransferase as a potential antimalarial target: inhibition studies using improved methods for enzyme production and assay. *Malar. J.* **2012**, *11*, 194.
(30) Cook, P. F.; Cleland, W. W. *Enzyme Kinetics and Mechanism*; Garland Science, 2007.
(31) Nutho, B.; Mahalapbutr, P.; Hengphasatporn, K.; Pattaranggoon, N. C.; Simanon, N.; Shigeta, Y.; Hannongbua, S.; Rungrotmongkol, T. Why are lopinavir and ritonavir effective against the newly emerged coronavirus 2019? Atomistic insights into the inhibitory mechanisms. *Biochemistry* **2020**, *59*, 1769−1779.
(32) Nutho, B.; Rungrotmongkol, T. Binding recognition of substrates in NS2B/NS3 serine protease of Zika virus revealed by molecular dynamics simulations. *J. Mol. Graph. Model.* **2019**, *92*, 227−235.
(33) Soniya, K.; Chandra, A. Free energy landscapes of prototropic tautomerism in pyridoxal 5′-phosphate Schiff bases at the active site of an enzyme in aqueous medium. *J. Comput. Chem.* **2018**, *39*, 1629−1638.
(34) Frisch, M. J.; Trucks, G. W.; Schlegel, H. B.; Scuseria, G. E.; Robb, M. A.; Cheeseman, J. R.; Scalmani, G.; Barone, V.; Petersson, G. A.; Nakatsuji, H.; Li, X.; Caricato, M.; Marenich, A. V.; Bloino, J.; Janesko, B. G.; Gomperts, R.; Mennucci, B.; Hratchian, H. P.; Ortiz, J. V.; Izmaylov, A. F.; Sonnenberg, J. L.; Williams-Young, D.; Ding, F.; Lipparini, F.; Egidi, F.; Goings, J.; Peng, B.; Petrone, A.; Henderson, T.; Ranasinghe, D.; Zakrzewski, V. G.; Gao, J.; Rega, N.; Zheng, G.; Liang, W.; Hada, M.; Ehara, M.; Toyota, K.; Fukuda, R.; Hasegawa, J.; Ishida, M.; Nakajima, T.; Honda, Y.; Kitao, O.; Nakai, H.; Vreven, T.; Throssell, K.; Montgomery, J. A., Jr.; Peralta, J. E.; Ogliaro, F.; Bearpark, M. J.; Heyd, J. J.; Brothers, E. N.; Kudin, K. N.; Staroverov, V. N.; Keith, T. A.; Kobayashi, R.; Normand, J.; Raghavachari, K.; Rendell, A. P.; Burant, J. C.; Iyengar, S. S.; Tomasi, J.; Cossi, M.; Millam, J. M.; Klene, M.; Adamo Cammi, C. R.; Ochterski, J. W.; Martin, R. L.; Morokuma, K.; Farkas, O.; Foresman, J. B.; Fox, D. J. *Gaussian 09*. revision C. 01; Gaussian, Inc: Wallingford, CT, 2010.
(35) Tian, C.; Kasavajhala, K.; Belfon, K. A. A.; Raguette, L.; Huang, H.; Migues, A. N.; Bickel, J.; Wang, Y.; Pincay, J.; Wu, Q.; et al. ff19SB: amino-acid-specific protein backbone parameters trained

https://doi.org/10.1021/acsomega.3c01309
ACS Omega 2023, 8, 35580−35591

against quantum mechanics energy surfaces in solution. *J. Chem. Theory Comput.* **2019**, *16*, 528−552.
(36) Case, D. A.; Betz, R. M.; Cerutti, D. S.; Cheatham, T. E.; Darden, T.; Duke, R.; Giese, T. J.; Gohlke, H.; Götz, A.; Homeyer, N. *Amber 2021*; University of California: San Francisco, 2021.
(37) Wang, J.; Wolf, R. M.; Caldwell, J. W.; Kollman, P. A.; Case, D. A. Development and testing of a general amber force field. *J. Comput. Chem.* **2004**, *25*, 1157−1174.
(38) Dolinsky, T. J.; Nielsen, J. E.; McCammon, J. A.; Baker, N. A. PDB2PQR: an automated pipeline for the setup of Poisson−Boltzmann electrostatics calculations. *Nucleic Acids Res.* **2004**, *32*, W665−W667.
(39) Case, D. A.; Betz, R. M.; Cerutti, D. S.; Cheatham, T. E.; Darden, T.; Duke, R.; Giese, T. J.; Gohlke, H.; Götz, A.; Homeyer, N. *Amber*; University of California: San Francisco, 2016; Vol. *16*.
(40) Miyamoto, S.; Kollman, P. A. Settle: An analytical version of the SHAKE and RATTLE algorithm for rigid water models. *J. Comput. Chem.* **1992**, *13*, 952−962.
(41) Ryckaert, J. P.; Ciccotti, G.; Berendsen, H. J. C. Numerical integration of the cartesian equations of motion of a system with constraints: molecular dynamics of n-alkanes. *J. Comput. Phys.* **1977**, *23*, 327−341.
(42) Roe, D. R.; Cheatham, T. E. PTRAJ and CPPTRAJ: software for processing and analysis of molecular dynamics trajectory data. *J. Chem. Theory Comput.* **2013**, *9*, 3084−3095.
(43) Cui, Q.; Sulea, T.; Schrag, J. D.; Munger, C.; Hung, M. N.; Naïm, M.; Cygler, M.; Purisima, E. O. Molecular dynamics−solvated interaction energy studies of protein−protein interactions: the MP1−p14 scaffolding complex. *J. Mol. Biol.* **2008**, *379*, 787−802.
(44) Naïm, M.; Bhat, S.; Rankin, K. N.; Dennis, S.; Chowdhury, S. F.; Siddiqi, I.; Drabik, P.; Sulea, T.; Bayly, C. I.; Jakalian, A.; Purisima, E. O. Solvated interaction energy (SIE) for scoring protein-ligand binding affinities. 1. Exploring the parameter space. *J. Chem. Inf. Model.* **2007**, *47*, 122−133.
(45) Miller, B. R. I. I. I.; McGee, T. D. Jr.; Swails, J. M.; Homeyer, N.; Gohlke, H.; Roitberg, A. E. MMPBSA.py: an efficient program for end-state free energy calculations. *J. Chem. Theory Comput.* **2012**, *8*, 3314−3321.
(46) Wolber, G.; Langer, T. LigandScout: 3-D pharmacophores derived from protein-bound ligands and their use as virtual screening filters. *J. Chem. Inf. Model.* **2005**, *45*, 160−169.
(47) Humphrey, W.; Dalke, A.; Schulten, K. VMD: Visual molecular dynamics. *J. Mol. Graph.* **1996**, *14*, 33−38.
(48) Yadava, U. Search algorithms and scoring methods in protein-ligand docking. *Endocrinol. Metab. Int. J.* **2018**, *6*, 359−367.
(49) Purisima, E. O. Fast summation boundary element method for calculating solvation free energies of macromolecules. *J. Comput. Chem.* **1998**, *19*, 1494−1504.
(50) Purisima, E. O.; Nilar, S. H. A simple yet accurate boundary element method for continuum dielectric calculations. *J. Comput. Chem.* **1995**, *16*, 681−689.
(51) Deetanya, P.; Hengphasatporn, K.; Wilasluck, P.; Shigeta, Y.; Rungrotmongkol, T.; Wangkanont, K. Interaction of 8-anilinonaphthalene-1-sulfonate with SARS-CoV-2 main protease and its application as a fluorescent probe for inhibitor identification. *Comput. Struct. Biotechnol. J.* **2021**, *19*, 3364−3371.
(52) Sanachai, K.; Somboon, T.; Wilasluck, P.; Deetanya, P.; Wolschann, P.; Langer, T.; Lee, V. S.; Wangkanont, K.; Rungrotmongkol, T.; Hannongbua, S. Identification of repurposing therapeutics toward SARS-CoV-2 main protease by virtual screening. *PLoS One* **2022**, *17*, No. e0269563.
(53) Adasme, M. F.; Linnemann, K. L.; Bolz, S. N.; Kaiser, F.; Salentin, S.; Haupt, V. J.; Schroeder, M. PLIP 2021: expanding the scope of the protein-ligand interaction profiler to DNA and RNA. *Nucleic Acids Res.* **2021**, *49*, W530−W534.
(54) Renwick, S. B.; Snell, K.; Baumann, U. The crystal structure of human cytosolic serine hydroxymethyltransferase: a target for cancer chemotherapy. *Structure* **1998**, *6*, 1105−1116.
(55) Ubonprasert, S.; Jaroensuk, J.; Pornthanakasem, W.; Kamonsutthipaijit, N.; Wongpituk, P.; Mee-udorn, P.; Rungrotmongkol, T.; Ketchart, O.; Chitnumsub, P.; Leartsakulpanich, U.; et al. A flap motif in human serine hydroxymethyltransferase is important for structural stabilization, ligand binding, and control of product release. *J. Biol. Chem.* **2019**, *294*, 10490−10502.

https://doi.org/10.1021/acsomega.3c01309
ACS Omega 2023, 8, 35580−35591